CLAS12 Forward Time-of-Flight at USC: A Comprehensive Update

Ralf Gothe, Evan Phelps, Robert Steinman, and Ye Tian

Department of Physics and Astronomy, University of South Carolina

(Dated: November 21, 2009)

Abstract

The CEBAF 12GeV upgrade requires enhancements to the existing CLAS detector in Hall B to achieve particle separation into the expanded kinematic range accessible by the electron beam. The time-of-flight (TOF) detector is the primary instrument for particle identification of CLAS. In tandem with the existing Panel-1A Forward Time-Of-Flight (FTOF), the longest counters of the proposed Panel-1B FTOF detector, must achieve a resolution of better than 95 ps in order to achieve the overall required time resolution of 80 ps. Initial investigations at the University of South Carolina have yielded full-bar time resolutions of 42 ps for 6 $cm \times 6\ cm \times 120\ cm$ counters, which extrapolates to significantly better than 95 ps for the longest counters of 400 cm.

In preparation for mass production of the 384 counters that will compose Panel 1B, processes for quality assurance, construction, testing, and tracking have been developed. The construction process is outlined, and the calibration and measurement methods underlying the quality assurance and testing processes are described.

I. INTRODUCTION

The time-of-flight subsystem of the CLAS detector in Hall B was designed to allow separation of pions and kaons in the kinematic range accessible with a 6-GeV electron beam by providing time resolutions from 90 ps to 160 ps at the forward angles, where the most energetic particles are detected.[1] To reliably separate p, π, and K in the kinematic range accessible with the proposed 11-GeV beam of the CEBAF upgrade, the FTOF detector must achieve a resolution of 80 ps[2] as illustrated in Fig. 1. This assumes a 4σ time difference between two particles, thus allowing for identification of a signal in the presence of other particles with a ten-fold higher rate.

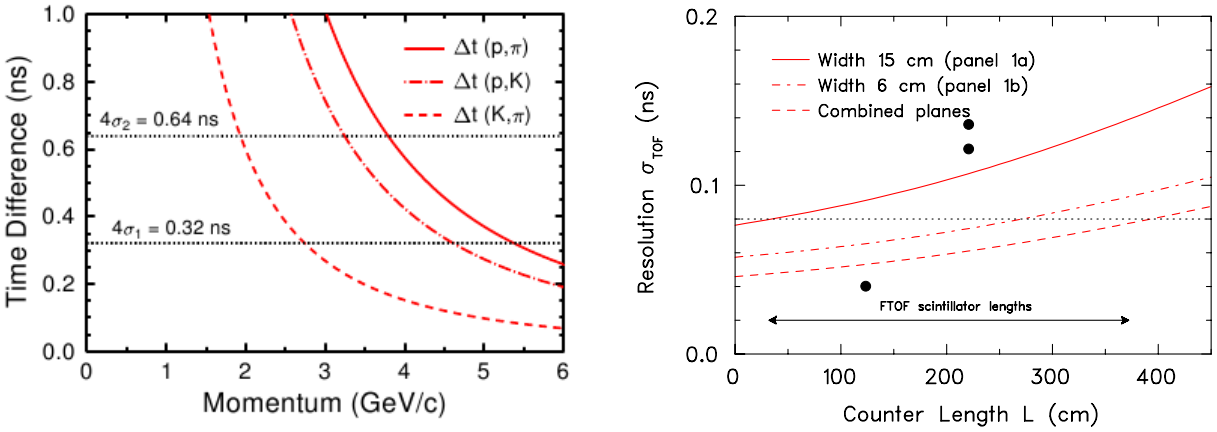

(a) Particle separation.

(b) Resolution curves.

FIG. 1: (a) The three curves indicate the time differences, Δt, between p/π, p/K, and π/K over the 650-cm path length from the target to Panel 1B.[2] σ_2 corresponds to Panel-1A counters; σ_1 corresponds to the Panel-1B counter resolution requirement. (b) The data point at (120cm,40ps) indicates a typical cosmic-ray resolution measurement of the prototype reference counters at the University of South Carolina (USC), whereas (213cm, 118ps) and further results as shown in Fig. 18(b) are prior cosmic-ray resolution measurements of Panel-1A counters as published in 1999.[1] The data point at (213cm, 138ps) indicates the resolution of a Panel-1B counter from JLab as measured by the system at USC in 2009.

As in the current 6-GeV FTOF detector (Panel 1A), each counter of the additional 12-GeV FTOF (Panel 1B) is composed of a long rectangular plastic scintillator with two cylindrical PMTs, one on each end, directly attached without light guides. The scintilla-

tor lengths are tightly constrained by the established six-panel FTOF geometry and the requirement that the new panels do not restrict the CLAS12 acceptance as defined by the other detector components, but the thickness and width, $6\,cm \times 6\,cm$, are selected to optimize photon statistics, geometric matching with the photocathodes, and closest possible stacking. Compared to the Panel-1A $5\,cm \times 15\,cm$ FTOF scintillators, the $6\,cm \times 6\,cm$ scintillators increase the number of photons produced by a factor of 6/5; the increased ratio of photocathode area to scintillator exit window area increases the number of photons that reach the photocathode by at least a factor of 25/12. Thus, disregarding that the area ratio factor acts on the number of photons after light attenuation, the Panel-1B scintillator geometry increases the number of photons reaching the photocathode by a factor of about 5/2 and, therefore, improves the resolution by a factor of $\sqrt{2/5}$, neglecting the resolution of any contributions that are independent of light level.

With a resolution of better than $150\,ps$ for the longest counters of Panel 1A, the Panel-1B counters must achieve resolutions better than $95\,ps$ for the combined resolution goal of $80\,ps$ to be reached (Fig. 1). Preliminary prototype results exceed this requirement.

II. COUNTER CONSTRUCTION

The construction process incorporates custom tools for consistency and precision in assembly, component and system tests for quality assurance, and a database application for automated analysis and quality tracking. The process begins with a visual inspection of the plastic scintillator, recording any inclusions, inhomogeneities, or defects. Each end of the scintillator is fitted with black tape, which masks the corners while leaving a circular window that extends one millimeter into the area that will be covered by the photocathode. The corner blocking provides two advantages: (1) it reduces the amount of reflected light contributing to the leading edge of the PMT signal, particularly for the short scintillators, and (2) in the case that a glued PMT must be removed, it offers protection to the scintillator and provides a fulcrum for the PMT removal tool.

Before attaching the PMT to the scintillator, the PMT is tested with a thin scintillator slice and a Sr-90 source for signal integrity, gain, HV requirements, and magnetic field shielding. To facilitate efficient assembly-line testing, the PMT is placed inside a prefabricated light-tight box inside the magnetic field of a Helmholtz coil. The black box is fixed in

various orientations for axial and transverse field tests. Without a magnetic field, the HV required for the PMT to generate a continuous anode signal distribution that dies out at about $300\,mV$, reflecting the continuous energy spectrum of the three-body β^- decay, is also determined. This HV corresponds to the approximate HV requirements for the PMT in the full experimental assembly of the three-bar time resolution measurements (Sec. VI A). The results for each PMT are stored in the testing database for tracking.

The scintillator is loaded onto the curing windmill, which holds up to six scintillators vertically. A centering tool is used to attach the PMT to the upward facing end of the scintillator, such that the glue can cure while the PMT-scintillator assembly is held upright. After twenty-four hours, the centering tool is removed, the scintillator is rotated 180°, and the process is repeated for the second PMT.

The bare counter is removed from the windmill to be wrapped with precision-cut aluminized Mylar and DuPont$^{\text{TM}}$Tedlar. The Tedlar film extends beyond each PMT onto the anode, dynode, and HV cables, providing a single light-tight encasing for the entire counter. The counter is loaded into the middle shelf of the three-bar cosmic ray resolution measurement system for a one-hour preliminary measurement followed by a twelve-hour comprehensive measurement, controlled by LabVIEW. All supporting histograms are automatically stored, and the results are programmatically analyzed and stored in the testing database for manual review and sign-off.

The verified counter is secured to its support structure by a series of tape loop points as described in *CLAS Time of Flight System Forward Angle Scintillator Construction Manual*[3]. In contrast to the assembly described in the manual, each Panel-1B support structure holds two counters. The assembly is finally stored until all are loaded and secured, one-layer deep, for delivery to JLab.

III. TDC TESTING

In a typical TOF detector, a photomultiplier pulse is transformed into a logic signal by a discriminator and its time of arrival is measured by a time-to-digital converter (TDC). Accordingly, the properties of the TDC determine the most basic unit of time resolution. Resolution, differential nonlinearity (DNL), and integral nonlinearity (INL), were measured for common-start CAMAC modules (Phillips Scientific PS7186 and Caen C414) and a newer

pipeline VME module (Caen V1290N). Neither CAMAC module met the manufacturer's specifications, but the Caen VME module V1290N performed acceptably, which was a major factor in the choice to use VME during our prototype development.

In order to determine the DNL profile of each module, a random start signal and periodic stop signal are fed to the TDC. The stop signal arrives at the TDC in any fixed-width time interval with equal probability. Thus, after a large number of events, a uniform distribution of counts per time interval (bin) is expected in the ideal case. Deviations from the ideal result reflect the TDC's DNL.

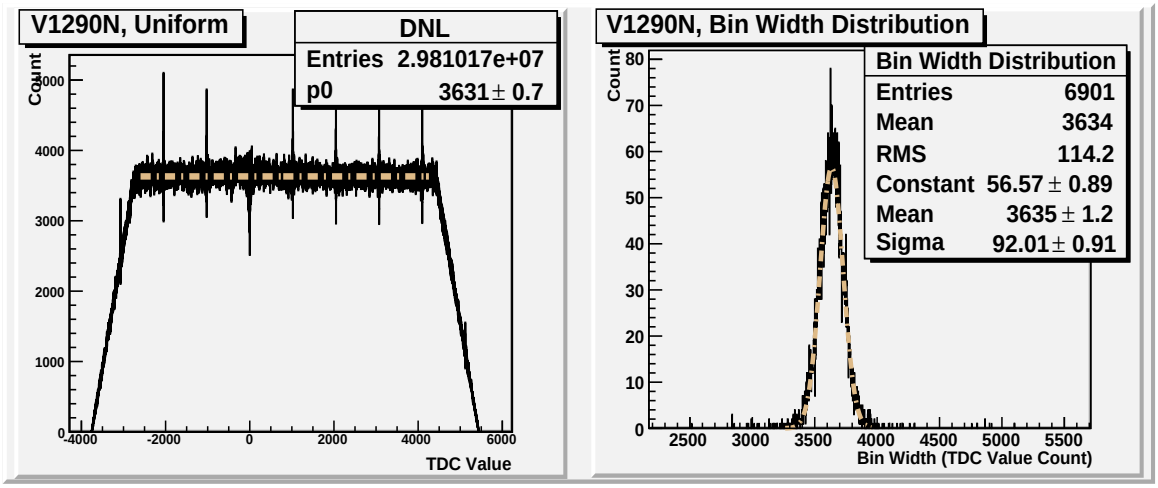

FIG. 2: The DNL histogram (left) deviates from an ideal uniform distribution, indicated by the dotted line, with a standard deviation of 92 counts (right), so the relative nonlinearity is $\frac{92}{3635} = 2.5\%$. After compensating for the statistical contribution of $\frac{\sqrt{3635}}{3635} = 1.66\%$, the relative DNL is 1.9%. The sloped edges result from the 25 ns variability in the V1290N's timing window with respect to the trigger. The periodic needles, again at 25 ns intervals, result from INL compensation on the TDC chip level.[4] The additional interference at TDC value 0 results from crosstalk between the two signals.

A radioactive source of Sr-90, placed on a counter, provides the random signals, which are converted to NIM logic signals by a leading edge discriminator (Phillips Scientific 705) for timing. In parallel, a timing unit (Phillips Scientific 794) provides logic pulses with a period greater than the TDC full range for the common-start CAMAC TDCs and a period of 200 ns for the pipeline VME TDC. The random signal serves as the reference signal, and the periodic signal, sent to all channels via a logic fan in/out (LeCroy 429A), serves

as the channel-specific stop. A TDC value distribution and its corresponding bin-width distribution are histogrammed in Fig. 2, and for comparison, the DNL histograms of PS7186 and C414 are illustrated in Fig. 3.

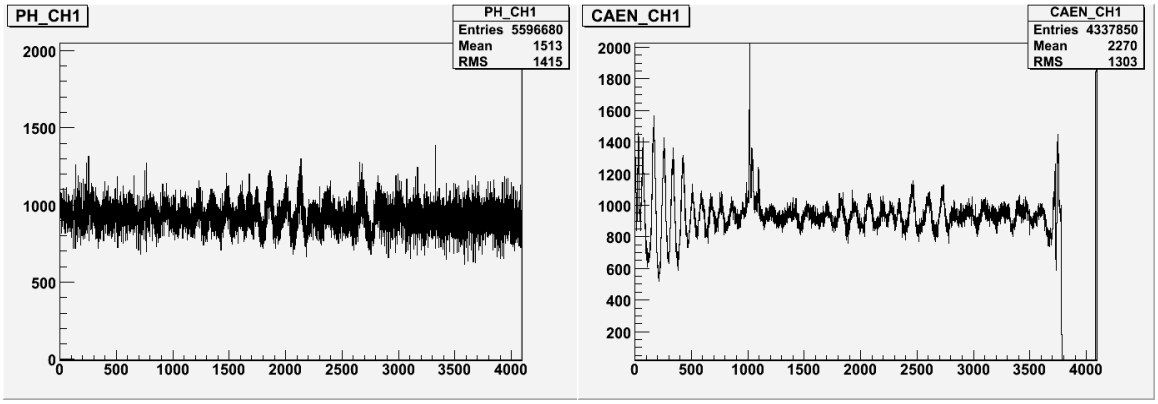

FIG. 3: DNL histograms for the Phillips Scientific 7186 (left) and the Caen 414 (right), compared with that of the Caen V1290N (Fig. 2, left), illustrate different nonlinearity signatures. The PS7186 and C414 are 12-bit CAMAC modules with limited ranges. The entire 100 ns range (12-bit) is usable in the PS7186, but the high nonlinearity below bin 1100 of the C414 restricts the usable range to only about 60 ns.

Calibration of the TDCs was accomplished by applying variable, oscilloscope-measured cable delays in 5 ns increments. Figure 4 demonstrates the calibration procedure where, in the illustrated case of the Caen C414, the average bin width is 25.11 ps with an offset of 2.8 ns. Each 5ns-interval peak includes 1000 entries and has a width corresponding to $0.6\,bins < \sigma < 0.8\,bins$. Results for each TDC are tabulated in Table I.

TABLE I: TDC Summary.

Model	DNL_σ	DNL_{max}	Range(ns)	Offset(ns)	Bin Size(ps)	Resolution(ps)
PS7186	9.8%	48.9%	100	18-21	24.98	19.0
C414	8.9%	135.6%	72	0-5	25.11	17.5
V1290N	1.9%	41.1%	N/A	N/A	24.75	32.5

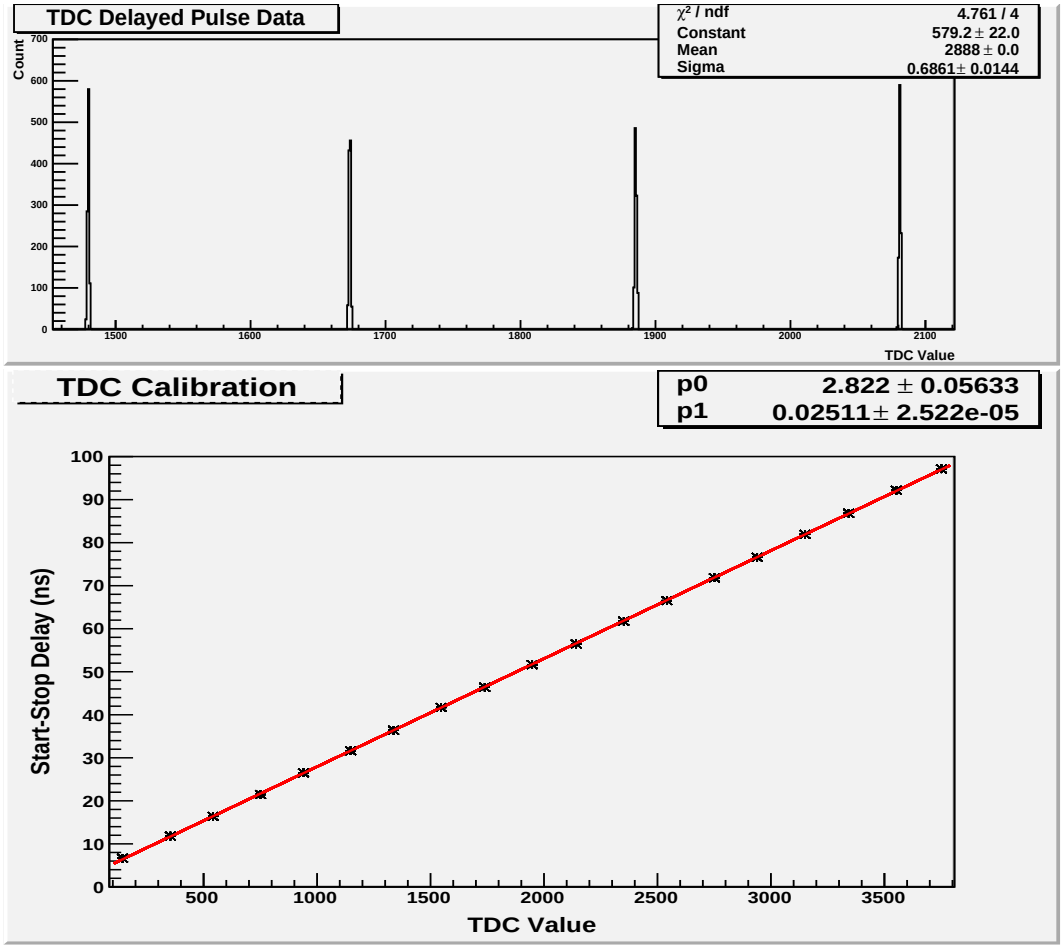

FIG. 4: Typical TDC calibration results illustrated for the Caen C414. Two copies of the same signal are used as start and stop times, with the latter being delayed with measured cable lengths in 5 ns increments (top). The typical peak width corresponds to $\sigma = 0.7\,bins$. The mean TDC value of each peak is plotted with its corresponding measured delay (bottom) to get the TDC sensitivity and offset (parameters $p1$ and $p0$, respectively).

IV. ADC TESTING

For the purpose of time resolution measurements, the ADC is only used in correcting for signal time of arrival, so calibrating the ADC values to an absolute energy scale of energy deposited is unnecessary. However, identifying the module's ground and the system charge offset (the *zero*) is crucial. For the prototype testing, the Caen V792N QDC[5] (integrating ADC) was tested and calibrated such that the zero was in an acceptable range using a combination of the module's software-adjustable pedestal and an externally applied DC

offset. To identify the full range of the ADC's pedestal, a fixed-width integration gate ($T_{gate} = 100\,ns$) and measured DC offsets are applied to a ground signal and integrated for various pedestal settings (Fig. 5).

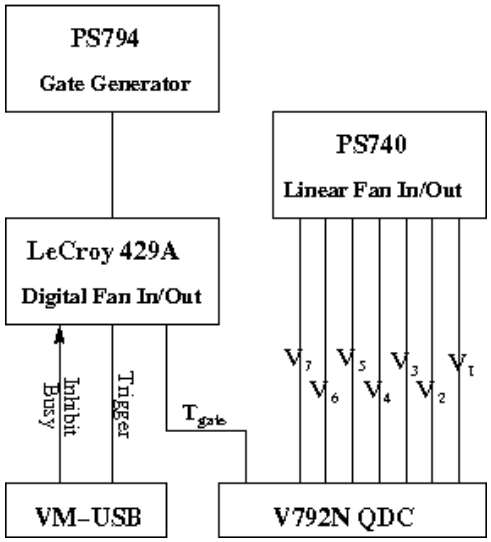

FIG. 5: A fixed-width integration gate, T_{gate}, and variable DC offsets, V_1-V_7 are used to calibrate the ADC, including sensitivity and pedestal measurements.

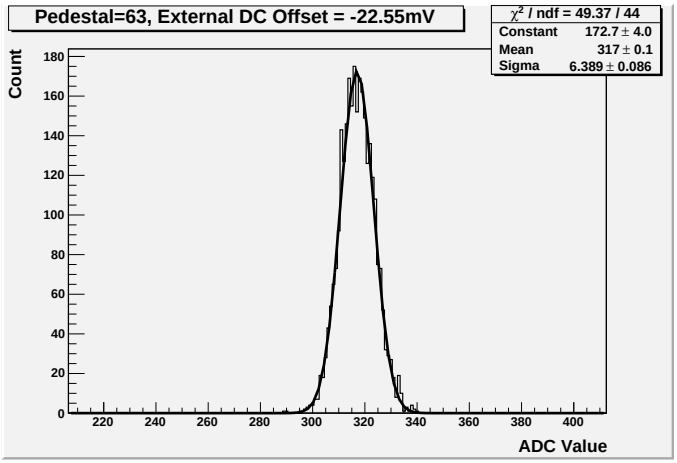

FIG. 6: An ADC distribution corresponding to a $-22.55\,mV$ offset integrated over $100\,ns$.

Figure 6 illustrates the ADC distribution when the pedestal is set to 63 and an external DC offset of $-22.55\,mV$ is applied. Combining such results for various DC offsets, the relationship between the DC offset and ADC value is determined (see Fig. 7(a)). The y-intercept of the best-fit line indicates the ADC's virtual ground, its pedestal current, with

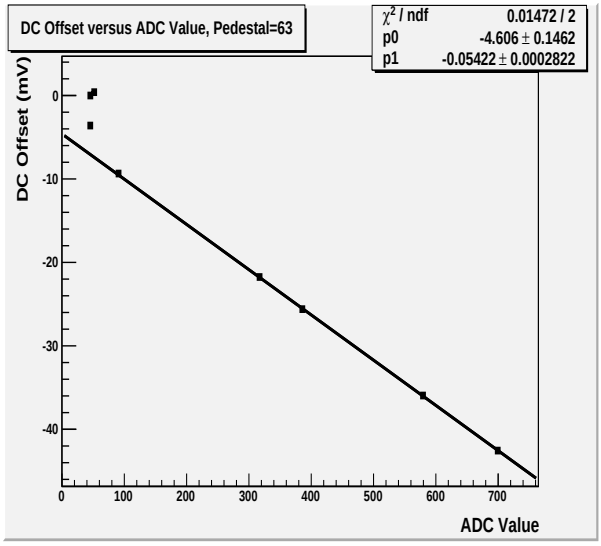

(a) DC offset versus ADC.

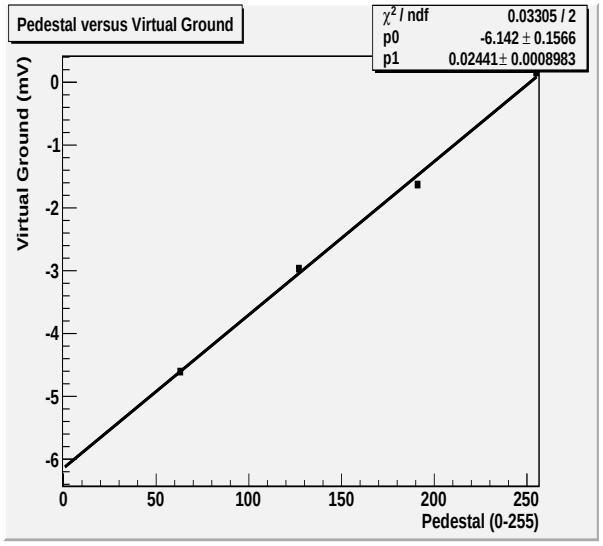

(b) Pedestal setting versus virtual ground.

FIG. 7: (a) For the adjustable pedestal setting of 63, the module has a virtual ground of $-4.6\,mV$ as determined by the ADC zero-crossing. (b) This zero-crossing varies from $\approx 0\,mV$ to $\approx -6\,mV$, so even in this case, an external DC offset is required to push the overall system offset into the active ADC range.

respect to which it integrates incoming signals. Finally, the module's pedestal settings are compared to the corresponding virtual ground values to determine the full range of the adjustable intrinsic pedestal, as shown in Fig. 7(b).

The sensitivity of the ADC is determined from Fig. 7(a), where the best-fit line is cast in terms of charge rather than DC offset as in equation (1), where Q corresponds to total charge, x to ADC value (bin), and R to resistance ($50\,\Omega$).

$$Q = \left(-4.606\,\frac{mV}{bin}x - 0.0542\,mV\right)\left(\frac{T_{gate}}{R}\right) = -9.2\,\frac{pC}{bin}x - 0.11\,pC \tag{1}$$

Accordingly, the V792N's sensitivity of $9.2\,\frac{pC}{bin}$ is consistent with the documented sensitivity of $10\,\frac{pC}{bin}$.

V. TIME-WALK CORRECTIONS

To mitigate the effect of time-walk on the resolution of the three-bar method (see Sec. VI A and, specifically, Fig. 15), a one-parameter time-walk correction is applied to each PMT. One PMT, the *reference* PMT ML (middle-left), determines the relative timing of all the other

signals. Accordingly, for a single relative time, two parameters (λ_i and λ_{ref}) must be used, as in Eq. (2),

$$t_{corrected} = \left(TDC_i - \frac{\lambda_i}{\sqrt{ADC_i}} \right) - \left(TDC_{ref} - \frac{\lambda_{ref}}{\sqrt{ADC_{ref}}} \right) \tag{2}$$

where both ADC values are corrected for the actual system offset. For each ionizing particle path, the time, with respect to a correlated trigger time, is ideally fixed, so the spreading of $t_{corrected}$ values on a specified path must be minimized with the two-parameter correction function. Figure 8, where the color scale represents the time spreading, illustrates this two-parameter minimization process.

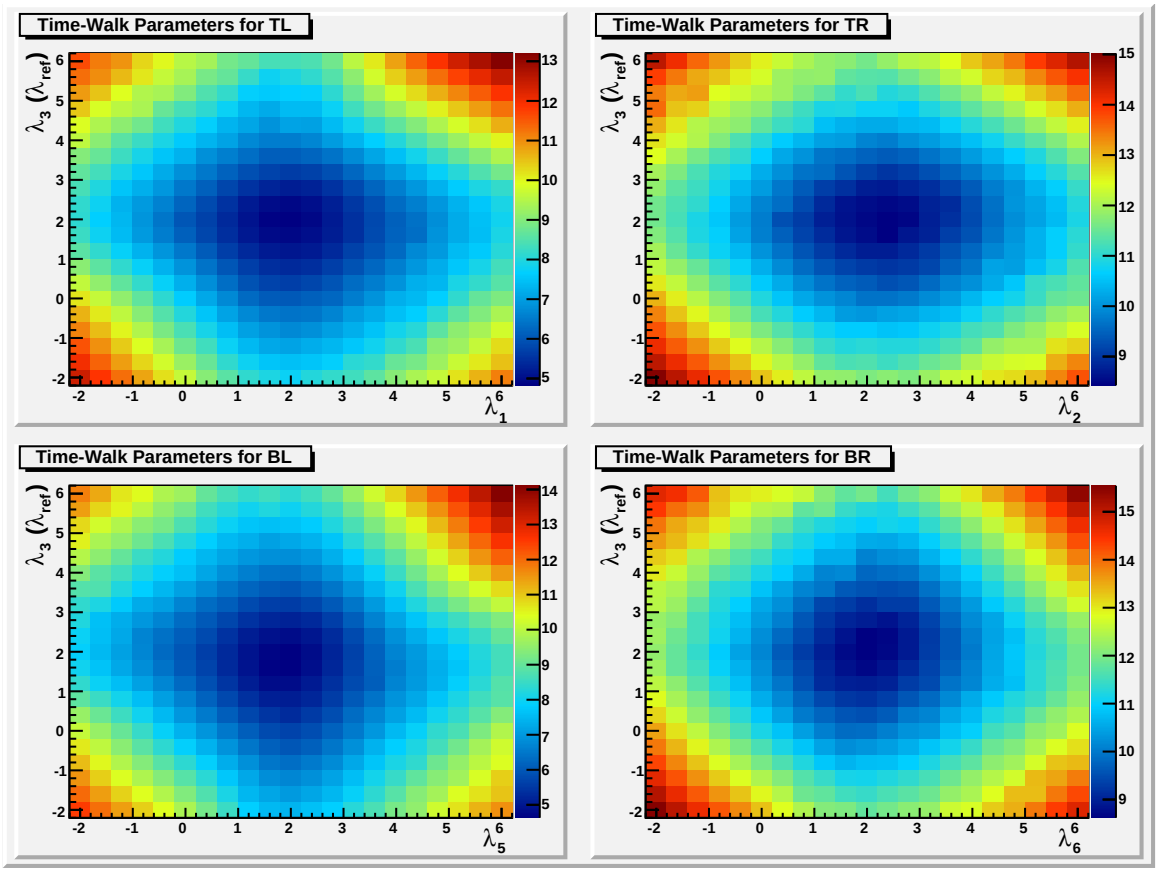

FIG. 8: For left and right PMTs of the top and bottom counters, a local minimum of the corresponding σ_i of TDC_i value distributions is identified. For example for the top-left PMT times (TDC_1), the distribution width is minimized at approximately (λ_1,λ_3) = (1.8,1.8).

The y-scale in each histogram of Fig. 8 represents the same reference bar parameter λ_3, so the minimum of each surface must have a common λ_3 within statistical tolerances. The

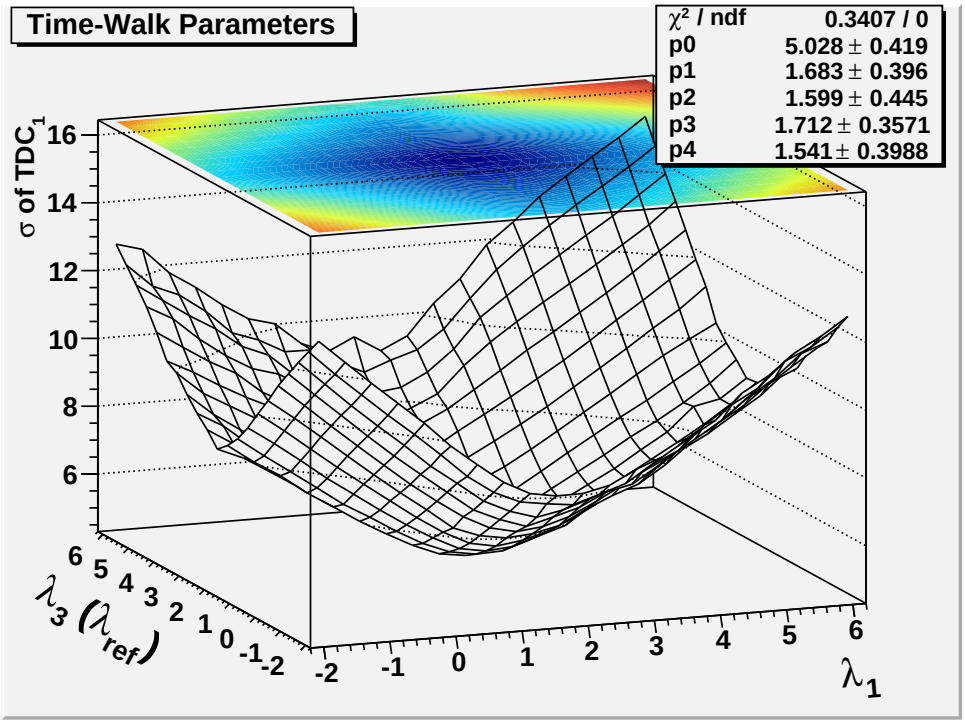

FIG. 9: The minimum is finally determined with a two-dimensional second-order polynomial fit. In this case, (λ_1,λ_3) = (1.7,1.7).

MR (middle-right) parameter corresponds to a PMT on the same counter as the reference time PMT, so the parameters λ_3 and λ_4 are correlated such that there is no local minimum (Fig. 10), but only a ridge whose slope changes with TDC difference (ultimately with ADC ratio). Since no local minimum is identifiable, λ_3 is defined by the minimum in the other histograms, and λ_4 is determined by the so fixed λ_3. The minimum is obtained for TDC difference values along the length of the counter, such that each of the six parameters is describable as a function of TDC difference or position (Fig. 11). These parameter functions, second-order polynomial fits to the data, are then used across the continuous length of the counter rather than at discrete positions.

VI. RESOLUTION MEASUREMENT METHODS

Three resolution measurement methods were evaluated – (1) the coordinate method, (2) the reference counter method, and (3) the three-bar cosmic ray method. The coordinate method, described in CLAS-NOTE 2004-016[6], uses a small Sr-90 source to measure position-

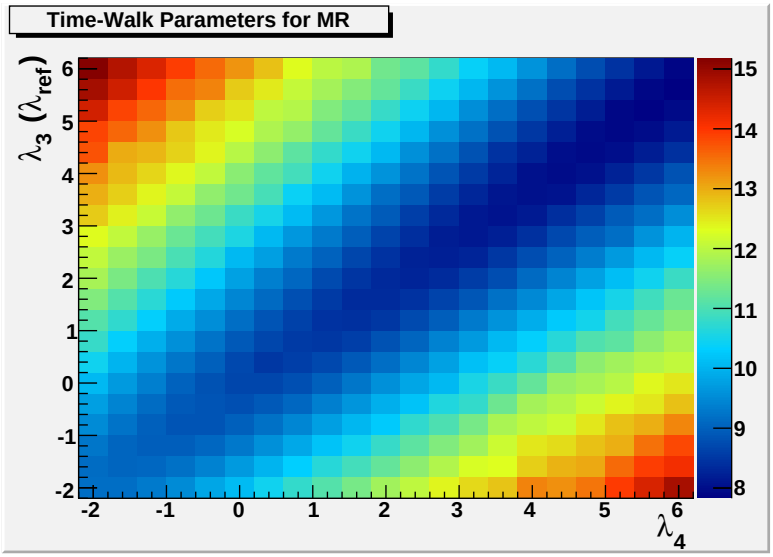

FIG. 10: The middle-bar parameters, $\lambda_{ref} = \lambda_3$ and λ_4, are correlated, hence no local minimum exists.

specific resolutions along the counter, but it is highly inappropriate for fast and reliable resolution measurements of 384 counters, since it involves multiple data runs for each counter at discrete positions, which have to be manually measured. Furthermore, the Sr-90 events are not representative of CLAS12 events, neither in penetration depth nor photon statistics. The reference counter method uses two thin scintillators to effectively collimate cosmic ray trajectories to perpendicularly traverse the counter at a fixed position, as shown in Fig. 12. This method suffers not only from the need for multiple data runs but more prohibitively from extremely low event rates. A variant of this method (see Fig. 13), in which a single thin scintillator is positioned between two longer scintillators achieving a partial collimation, was also evaluated. The positions on top and bottom scintillators are further restricted by cutting away low ADC events on the middle bar, thus reducing the number of particles traveling along non-vertical paths. However, this method suffers still from very low event rates and the need for multiple measurements across the length of a counter. The three-bar cosmic ray method, however, resolves all of these issues.

A. Three-Bar Cosmic Ray Method

The three-bar cosmic ray method has three primary advantages: a high event rate, a symmetry that allows for the collective treatment of all particle paths, and an energy deposit

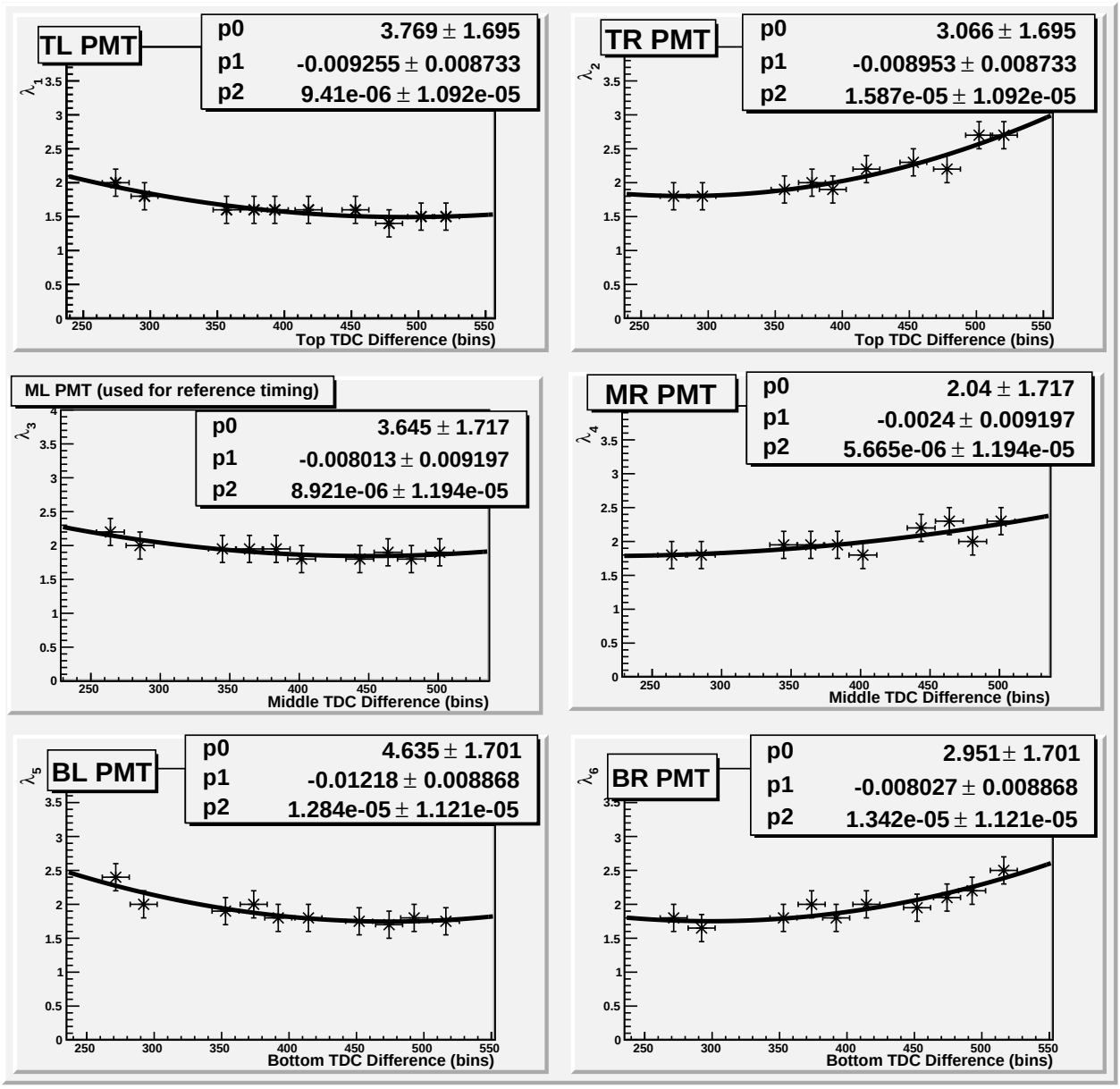

FIG. 11: The six parameters, λ_1-λ_6 are determined for various TDC difference values (corresponding to positions on each counter). Each is fit with a second-order polynomial and used as a function for the full-bar resolution determination.

per particle similar to CLAS12 experimental conditions. The configuration includes three equally spaced counters – two reference counters, top and bottom, of known resolution, and an exchangeable middle counter to be examined. Figure 14 illustrates the counter configuration and indicates two possible particle paths. The equal vertical spacing of the counters guarantees that $T \equiv \frac{t_t+t_b}{2} - t_m = const$ independent of particle path, where t_t, t_m,

FIG. 12: In the reference counter method, 5mm-thin scintillators are placed above and below the counter to be tested so that the position of cosmic ray events on the middle counter is fixed. The TDC difference between left and right PMTs on the middle counter is then used to determine the counter's resolution.

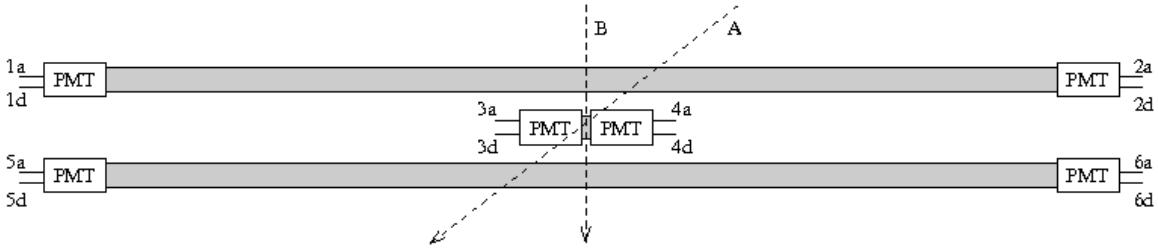

FIG. 13: This variant of the reference counter method does not physically restrict particles to pass through vertically (path B), because particles along path A also triggers all six PMTs. However, paths such as A are further reduced by cutting away middle-bar low ADC values, which correspond generally to particles traveling through less than the 5-cm vertical extent of the middle scintillator.

and t_b denote the time the particle passes through the top, middle, and bottom counters, respectively.

In terms of basic time measurements, t_i (the time of PMT signal i) and t_{ref} (the reference

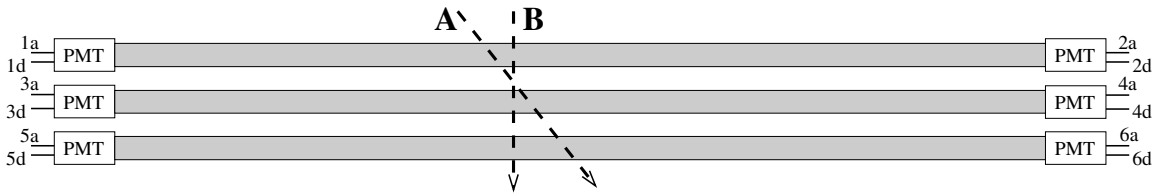

FIG. 14: Paths A and B represent two possible ionizing particle paths. The three counters are equally spaced such that any path between top and bottom counters is bisected by the middle counter.

time), t_t, t_m, and t_b can be written as follows:

$$\begin{aligned} t_t &= \frac{t_{tl}+t_{tr}}{2} = \frac{t_1+t_2-2t_{ref}}{2} \\ t_m &= \frac{t_{ml}+t_{mr}}{2} = \frac{t_3+t_4-2t_{ref}}{2} \\ t_b &= \frac{t_{bl}+t_{br}}{2} = \frac{t_5+t_6-2t_{ref}}{2} \end{aligned}$$

Accordingly, all reference time values in T cancel.

$$\begin{aligned} T &= \frac{t_1+t_2+t_5+t_6-4t_{ref}}{4} - \frac{t_3+t_4-2t_{ref}}{2} \\ &= \frac{t_1+t_2+t_5+t_6}{4} - \frac{t_3+t_4}{2} \end{aligned} \tag{3}$$

The spreading of T, quantified by its standard deviation σ_T, is then related to σ_i, the standard deviation of time measurements from PMT i, by $\sigma_T^2 = \frac{1}{16}(\sigma_1^2+\sigma_2^2+\sigma_5^2+\sigma_6^2)+\frac{1}{4}(\sigma_3^2+\sigma_4^2)$. Each counter is composed of the scintillator and two identical PMTs, which justifies the assumption that each of the two time measurements from one counter contribute equally to the resolution of the counter – i.e., $\sigma_{1,2} \equiv \sigma_1 = \sigma_2$, $\sigma_{3,4} \equiv \sigma_3 = \sigma_4$, and $\sigma_{5,6} \equiv \sigma_5 = \sigma_6$. Furthermore, the reference counters (top and bottom counters) are identical, so $\sigma_{1,2} = \sigma_{5,6}$. Finally, since $\sigma_{counter} = \frac{1}{\sqrt{2}}\sigma_{PMT}$, the resolution of the middle counter under evaluation is determined in terms of the measured σ_T and the known resolution, $\sigma_r = \frac{1}{\sqrt{2}}\sigma_{1,2}$, of each reference counter.

$$\begin{aligned} \sigma_T^2 &= \frac{1}{16}4\sigma_{1,2}^2 + \frac{1}{4}2\sigma_{3,4}^2 \\ \sigma_T^2 &= \frac{1}{16}4(\sqrt{2}\sigma_r)^2 + \frac{1}{4}2(\sqrt{2}\sigma_m)^2 \\ \sigma_T^2 &= \frac{1}{2}\sigma_r^2 + \sigma_m^2 \\ \sigma_m &= \sqrt{\sigma_T^2 - \frac{1}{2}\sigma_r^2} \end{aligned} \tag{4}$$

B. Electronic Configuration

The electronic configuration provides in-situ ADC offset measurements via an uncorrelated gate with a frequency of about one tenth of the event frequency, where an event requires a six-fold coincidence of all PMT signals. The anode signals are used for timing, while the dynode signals are used for ADC measurements. The VME controller executes an on-board stack and stores module data in buffers, which are read by a LabVIEW data acquisition application.

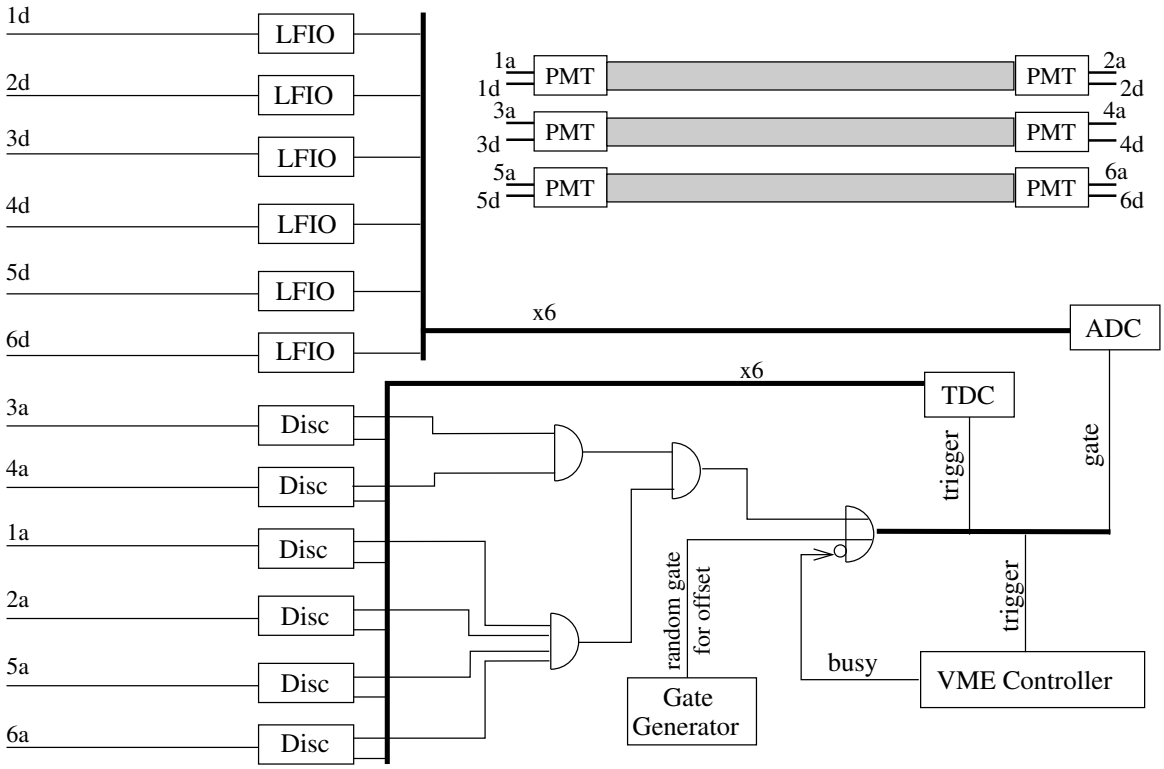

FIG. 15: The six PMTs of the three counters are labeled 1-6 from top-left to bottom-right. Each provides an anode and dynode signal, labeled as a and d, respectively. The six-fold coincidence is setup so that PMT 3a, the middle-left PMT, provides the reference time.

As illustrated in Fig. 15, each dynode signal passes through a Linear Fan-In/Fan-Out (LFIO), which provides a DC offset determined by the ADC virtual ground (Fig. 7(b)) and threshold. The anode signals are transformed into NIM logic signals by LeCroy 623B Leading Edge Discriminators, and coincidence logic is provided by Phillips Scientific (PS) 755 Quad Logic and LeCroy 622 Coincidence units. The final coincidence triggers the VME modules. The V1290N pipeline TDC is triggered to record signals arriving directly from the

discriminators, reducing the electronic resolution contribution to that of the discriminator jitter and the TDC, while the V792N QDC receives a 100 ns integration gate in which all signals of the event arrive.

C. Three-Bar Results

To determine the time resolution of the reference counters, the three-bar cosmic ray method is employed with three identical reference counters – three 6 cm × 6 cm × 120 cm Bicron BC-404 scintillators (Table II(b)) with Hamamatsu R9779 PMTs (Table II(a)) – so that Eq. (4) reduces to $\sigma_{ref} = \sqrt{\frac{2}{3}}\sigma_T$. The analysis steps include calibration, event selection, time-walk corrections, and resolution determination. The calibration consists of identifying and adjusting the ADC offset, which is set to the lowest value possible without interfering with the ADC threshold. In the example of Fig. 16(a), the offset is seen at ADC value 63. The second peak, seen in Fig. 16(b) at 150, corresponds to the threshold of the discriminator. The event selection includes reducing the number of particles whose paths do not traverse at least the full 6cm thickness of each scintillator, which is accomplished by cutting away the events with ADC values lower than the low edge of the Landau-like portion of the ADC distribution of Fig. 16(b) at 750. Additional event selection cuts, such as the low-ADC cut in a position-dependent manner or cuts that reduce high angle trajectories to better emulate the transverse particle paths in CLAS, can further improve resolution results, but these cuts were not implemented in achieving the results quoted herein.

TABLE II: Manufacturers' specifications for PMTs and scintillators.

(a) PMTs

PMT	Rise Time (ns)
XP2262B	2.0
R2083	0.7
R9779	1.8

(b) Scintillators

Scintillator	Bulk λ (cm)	τ (ns)
BC-408	380	2.1
BC-404	160	1.8
BC-418	100	1.4

The time-walk correction procedure requires position-dependent measurements of resolution (see Sec. V), which requires additional event selection for each position, or more appropriately, for each TDC difference. The choice of size for position segments involves a balance between refining localization and maintaining sufficient statistics. In this case, the

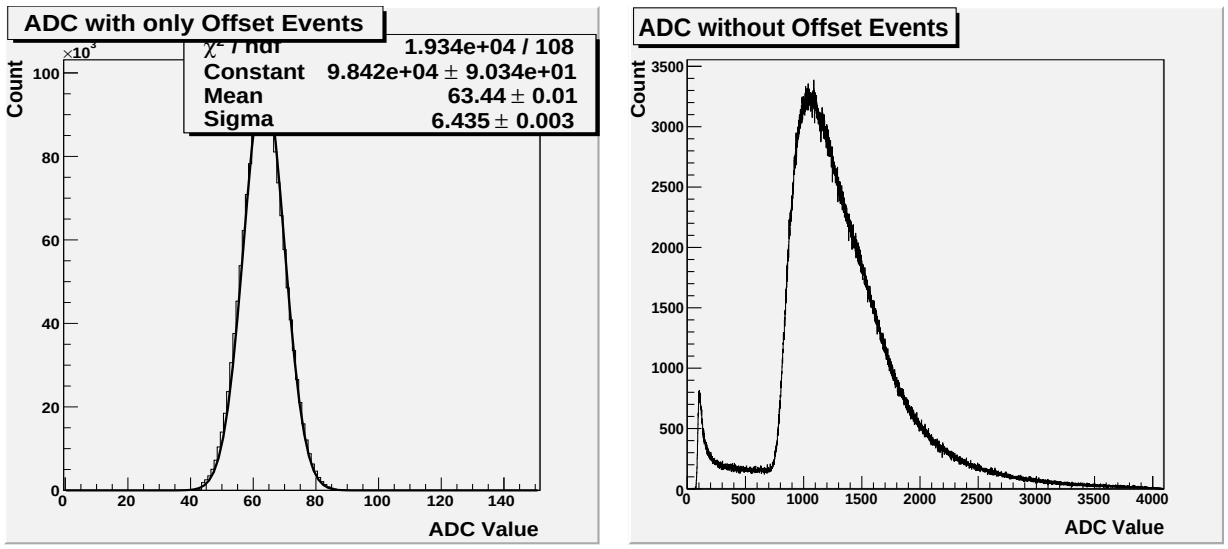

(a) ADC distribution of the offset.

(b) ADC distribution of cosmic ray events.

FIG. 16: (a) The ADC distribution corresponding only with the random gate is used to determine the ADC offset with respect to which the ADC values are corrected for time-walk correction purposes. (b) The uncorrected ADC distribution of the non-offset events shows a low discriminator threshold peak and a convoluted Landau distribution characteristic of the cosmic ray events.

segments include 20 TDC bins (approximately, 500 ps and 10 cm), where the cut is applied on the top and bottom counters such that only events corresponding to low-angle particle paths (vertical) are included. This low-angle selection is only a by-product of isolating the same position segment through all three bars and does not apply in the full-bar resolution case.

The position-dependent resolution for the reference counters ranges from 38 ps to 42 ps, and the full-bar resolution without any vertical particle path cuts, as illustrated in Fig.17(b), is $\sigma_{ref} = \sqrt{\frac{2}{3}}(2.085\, bins \cdot 25\, \frac{ps}{bin}) = 42.6\, ps$ after applying the position-dependent time-walk corrections.

D. Verification of Method

A $5\,cm \times 15\,cm \times 213\,cm$ Panel-1A counter (BC-408 scintillator, Photonis XP2262 PMTs), documented to have a resolution of about 118 ps in 1999, is used to verify the procedure. With two different sets of reference counters – $6\,cm \times 6\,cm \times 120\,cm$ and $5\,cm \times 5\,cm \times 400\,cm$ – the position-restricted time resolution of the counter has been determined, according to

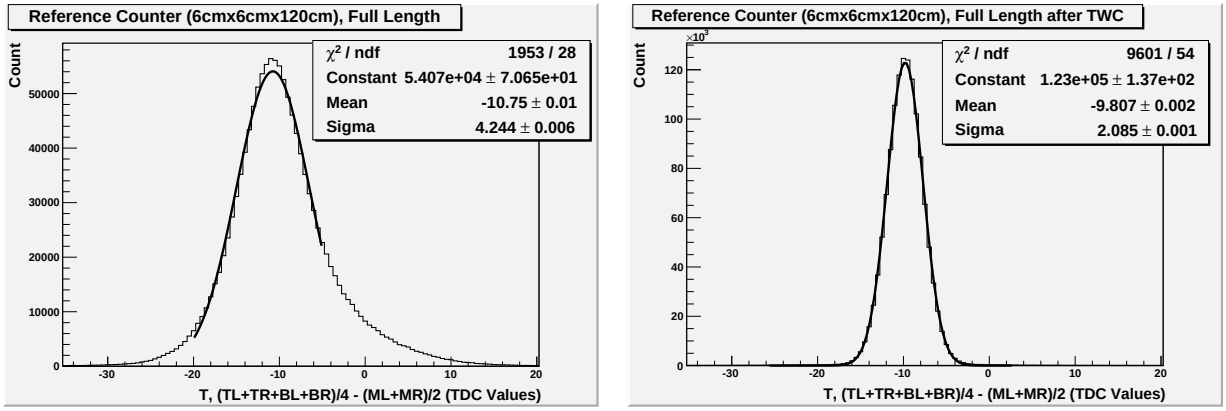

(a) Before time-walk correction.

(b) After time-walk correction.

FIG. 17: Reference counter resolution. (a) Across the entire 120-cm length of the reference counter, the resolution is $\sqrt{\frac{2}{3}}(4.244\,bins \cdot 25\,\frac{ps}{bin}) = 86.6\,ps$. (b) After applying the full-bar time-walk corrections, the resolution is improved to $42.6\,ps$.

Eq. (4), to be $138\,ps$, which is about $20\,ps$ worse than the 1999 measurement (Fig. 18). The time resolution degradation is due in part to a decrease in totally reflected light caused by the original aluminum wrapping adhering directly to the scintillator, as noted during the process of inspecting and re-wrapping the counter.

VII. CABLE ATTENUATION

The primary concerns regarding choice of cable type are cost, space, and impact on time resolution. Low-attenuation cables that maintain signal integrity over long distances cost more and occupy more space. With the cables of 768 PMTs being routed between the layers and panels of the detector, the extra volume of bundled cables is a serious concern, so barring an impact on time resolution, the thinner and less expensive RG58 cables are preferred.

The distortion and attenuation of signals through five different types of cable was investigated, including specification measurements of signal speed, attenuation, and rise time. Additionally, and most importantly, basic time resolution tests were performed for various lengths of cable. With a significant rise in time resolution between 100 ft and 200 ft of RG58 cable (Fig. 19), the prospect of centralizing all electronics is incompatible with the choice to use RG58 cable. However, with the digitization electronics at the panel edges, the maximum cable lengths would be under 21 ft, for which RG58 is still well-suited.

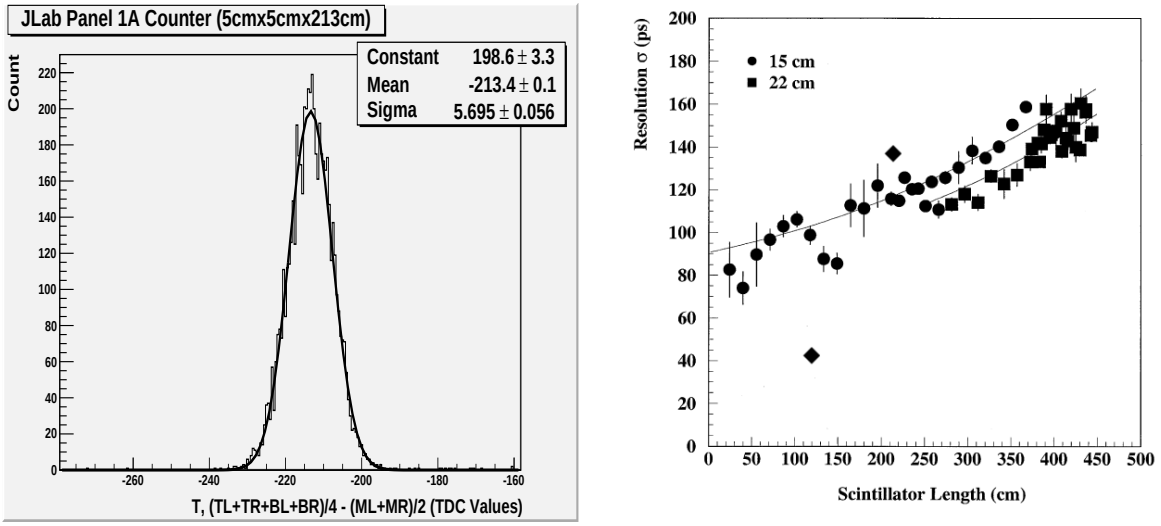

(a) Panel-1A counter resolution, 2009. (b) Cosmic ray tests for Panel 1A, 1999.

FIG. 18: (a) Time-walk-corrected cosmic ray test of a $5\,cm \times 15\,cm \times 213\,cm$ Panel-1A detector at USC in 2009 determined the resolution to be $138\,ps$. (b) The resolution of Panel-1A counters as measured by cosmic ray tests at JLab in 1999. The diamond-shaped data points at $(120cm, 42ps)$ (CLAS12 prototype) and $(213cm, 138ps)$ (CLAS6 15-cm counter) represent two recent USC results.

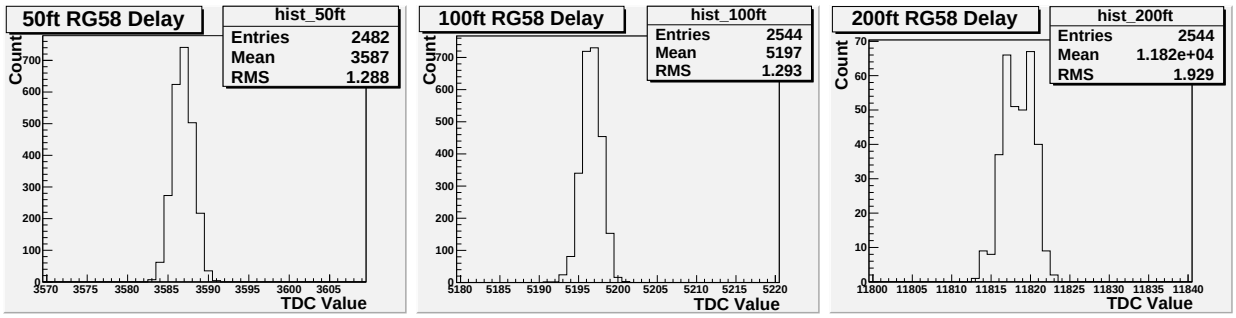

(a) 50 ft. (b) 100 ft. (c) 200 ft.

FIG. 19: The time resolution remained within the 30 ps to 35 ps TDC resolution until a 50% increase between 100 ft and 200 ft of RG58 cable delay.

VIII. μ-METAL SHIELDING

The Panel-1B PMTs must be properly shielded from the stray magnetic fields of the CLAS12 torus magnet,[2] which according to the latest stated estimates, will reach about 10 G (gauss). However, older simulations estimated fields of over 20 G for Panel-1B PMTs at the largest polar angles, so the magnetic field is a risk item until an official field magnitude

is provided.

In general, measurements show a loss in signal strength for PMTs in the presence of both axial and transverse magnetic fields[7]. To further investigate the impact of magnetic fields on different PMTs and shielding scenarios, various PMT assemblies were placed inside a uniform magnetic field created by a Helmholtz coil. The behavior of different 2-*in* PMTs (Photonis: XP2020, XP2020UR, XP20YO, XP20DO, Hamamatsu: R9779, and Electron Tubes: 9214A) is very similar. For geometric acceptance driven reasons and best time resolution results, investigations presented here focus on Hamamatsu R9779 assemblies. These still varied by shielding, which included cylindrical tubes and rectangular boxes of various thicknesses, as well as an R9779 variant with factory-installed shielding. The rectangular shields offer several advantages over the cylindrical shields. The rectangles match the scintillator spacing so each inner wall not only contributes to the shielding of each PMT itself but also to that of its direct neighbors, and by adding additional outer plates, the thickness is variable in the absence of geometric constraints. The box design also allows for one side to be removed so that cables can pass through notches sized for the cables rather than requiring space for the connectors to pass, as demanded by the cylindrical design. Each shield must end at the scintillator-to-photocathode junction, since otherwise the acceptance would be reduced. This requirement unfortunately also mitigates the effectiveness of axial field shielding.

In the presence of a 10-G transverse magnetic field, the unshielded PMTs lose all signal. However, with factory-installed shielding or 1 mm of encasement shielding, cylindrical or square, the 10-G transverse magnetic field does not affect the signal amplitude or shape. The 10-G axial field causes an unavoidable but not detrimental signal reduction of less than 10%. These results are illustrated in Fig. 20. However, there is a rapid deterioration in the signal strength under axial magnetic fields above $10\,G$ and under transverse fields above $20\,G$. Accordingly, additional shielding will be needed if the magnetic fields are to exceed either of these values. Transverse fields are easily shielded by additional μ-metal, which does not help in the case of axial fields, since no shielding can be extended beyond the crucially impacted photocathode. As described in Sec. II, these basic shielding tests, among other PMT tests, are performed on each PMT to ensure that they are effectively μ-metal shielded and meet all requirements and quality standards.

While the signal integrity measurements already suggest that the time resolution is not affected for shielded PMTs in transverse fields up to $20\,G$ and axial fields up to $10\,G$, direct

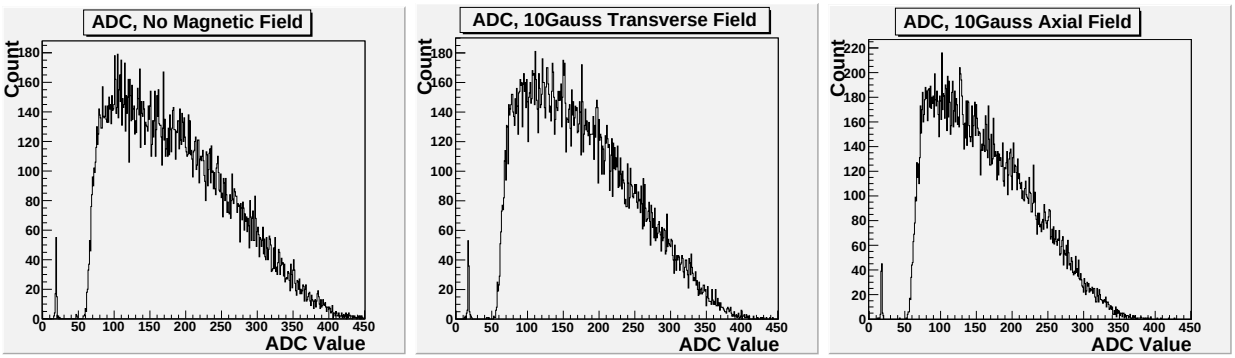

(a) No Magnetic Field. (b) 10-G Transverse Field. (c) 10-G Axial Field.

FIG. 20: The ADC distributions with no magnetic field and for a 10-G transverse field for the Hamamatsu shielded R9779 PMT are similar. The distributions with a 10-G axial field presents a 10% reduction in mean value. The small peak around ADC value 20 is the system offset.

time resolution tests in the presence of magnetic fields were carried out. For this purpose, the aforementioned three-bar cosmic ray method was performed with the addition of a Helmholtz coil surrounding the three right-side shielded R9779 PMTs. The time resolution of 40 ps remained unchanged for the cases of 0-G, 10-G transverse and axial, and 20-G transverse fields. However, axial magnetic fields of 10 G and higher adversely affect the time resolution and require active shielding to compensate the penetrating axial fields.

IX. SCINTILLATOR ATTENUATION LENGTH

The scintillator material for the TOF system must have short decay times, long attenuation length, and good spectral match to the PMTs. Initial measurements show that attenuation length values vary even among scintillation bars of the same material and from the same mold, so in order to verify that each counter meets required specifications, the attenuation length measurement is incorporated into the unit testing of each counter constructed for Panel 1B. The method uses the same data collected in the three-bar time resolution measurements described in Sec. VI B.

The attenuation length of scintillator can be divided into two parts. One part is called the *technical attenuation length* (TAL), which is defined as the length reducing the amount light by a factor e and which depends on the geometry the scintillator and the reflective properties of its surface. The other part is called *bulk attenuation length* (BAL), which

reduces the initial light intensity by a factor e according to the Buger-Lambert Law and which depends on the transparency and the scintillation material.

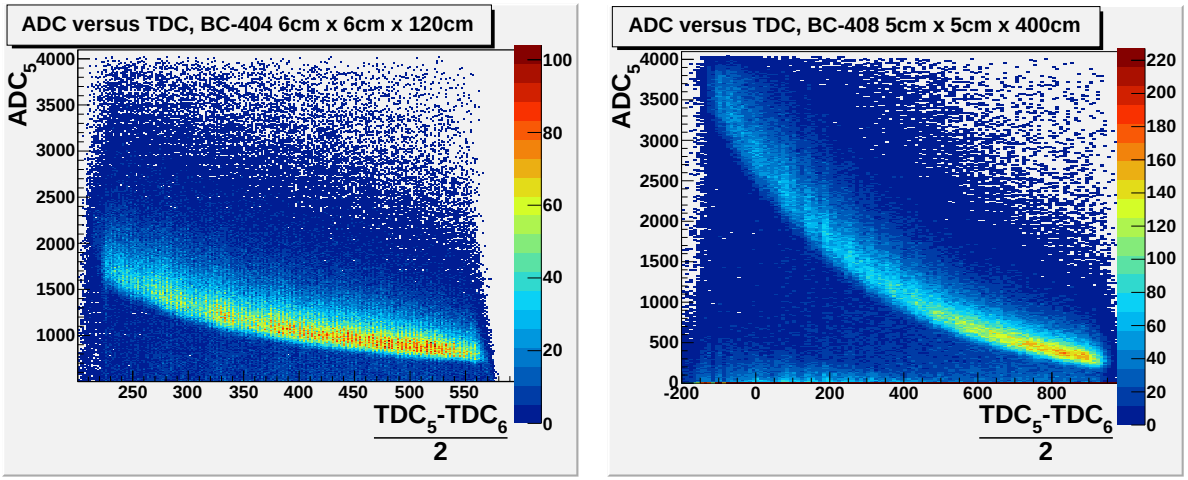

(a) ADC versus TDC difference for a $6cm\ x\ 6cm\ x\ 120cm$ BC-404 scintillator.

(b) ADC versus TDC difference for a $5cm\ x\ 5cm\ x\ 400cm$ BC-408 scintillator.

FIG. 21: Offset-corrected ADC values, which are directly proportional to the number of photons arriving at the photocathode are plotted against TDC difference values ($\frac{TDC_L - TDC_R}{2}$), which are proportional to the position through which the ionizing particles pass. To find the maximally occurring ADC value for each Δt slice, ADC distributions for each TDC difference interval are fit with Gauss-convoluted Landau functions.

The ADC provides a measure of the number of photons reaching the photocathode, and the left and right TDCs provide the time information needed to reconstruct the impact position based on the effective speed of light in the scintillator. The attenuation length parameters, TAL and BAL, of the scintillator are given by,

$$N = N_{0T} e^{-\frac{x}{\lambda_T}} + N_{0B} e^{-\frac{x}{\lambda_B}}, \tag{5}$$

where $N_0 = N_{0T} + N_{0B}$ is the initial number of photons caused by the cosmic ray passing through the scintillator at the impact position x and N is the number of photons arriving at the PMT. Figure 21 illustrates the relationship between ADC and TDC difference values for all data. Slices of the TDC difference values are projected onto the ADC axis, and fit with Gauss-convoluted Landau functions from which the most probable ADC value for each position is obtained (Fig. 22). These new pairs of data points are fit by various ansätze of exponential functions to extract the attenuation length parameters, as shown in Fig. 23.

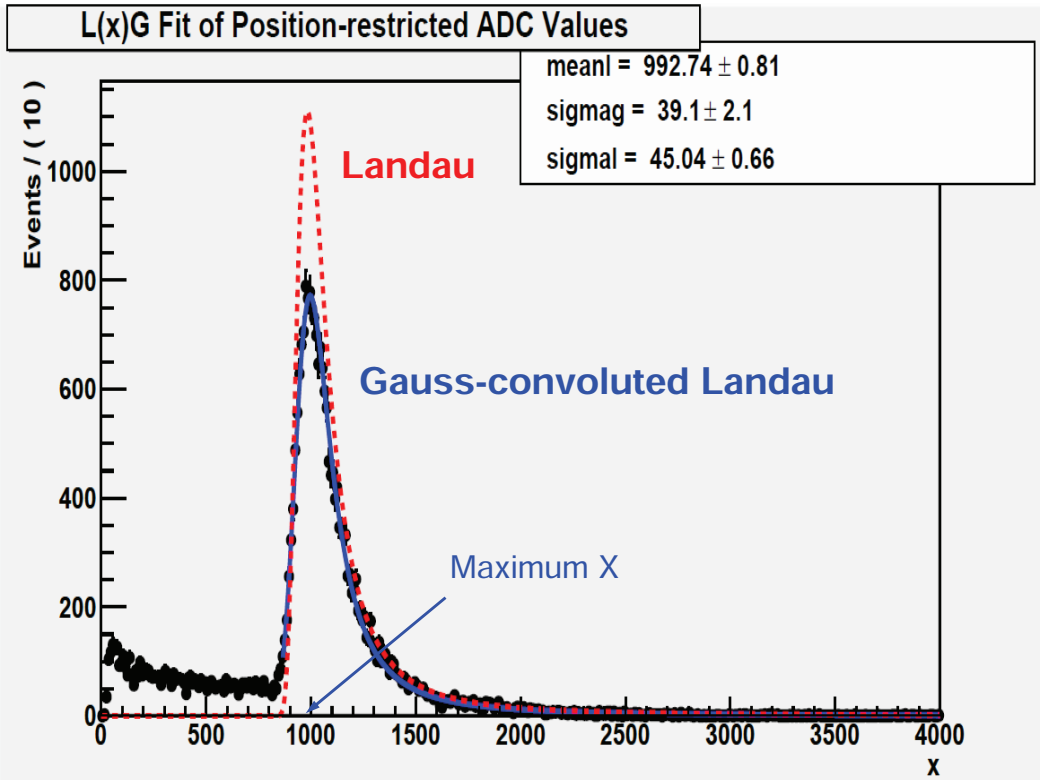

FIG. 22: Gauss-convoluted Landau fit of the ADC distribution for a central single TDC difference slice of 40 *bins* for the BC-404 120 *cm*-long bar, where x represents the ADC value, and "Maximum x" is hence the most probable ADC value.

With this method, the extracted BAL for the 5 cm × 5 cm × 400 cm BC-408 scintillator, (274.25 ± 8.05) cm, is too low, but the Eljen EJ200 scintillator of the same dimensions has an even lower BAL of (202.39 ± 7.89) cm, if compared to the factory specification of 380 cm (Table II(b)). Whereas the BAL of the 6 cm × 6 cm × 120 cm BC-404 scintillator, (327.90±53.27)cm, is significantly higher than the factory specification of 160cm (TableII(b)) while its TAL, (31.97 ± 5.27) cm, is as expected. These results further underline the need for close quality assurance measurements of the attenuation length.

X. CONCLUSIONS AND OUTLOOK

The USC TOF12 participants have successfully achieved and surpassed all design requirements and have developed testing, verification, and construction procedures for each major piece of the system. The primary efforts are currently focused on automating the

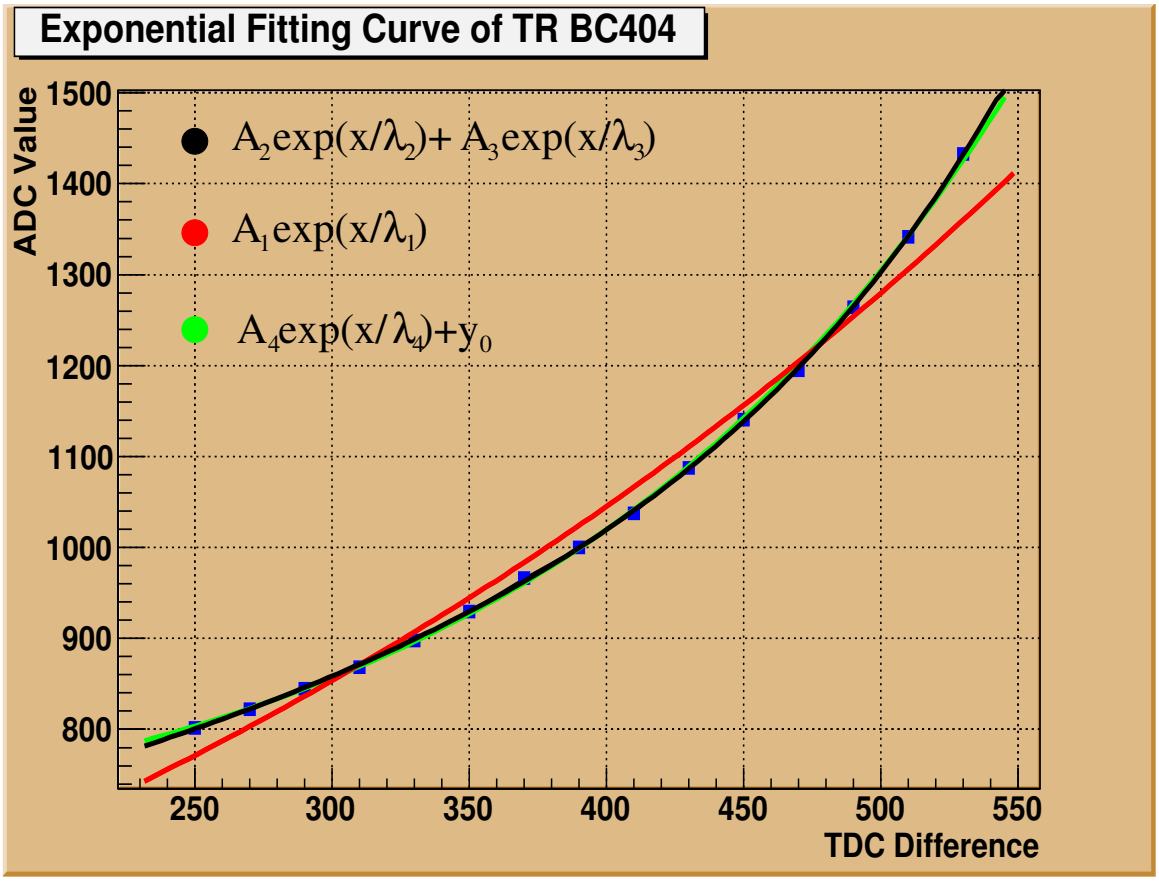

FIG. 23: ADC versus TDC difference for the right PMT of the BC-404 120 *cm*-long bar.

software procedures, establishing a database for tracking the performance of each detector component, building the needed construction tools, and optimizing the construction process.

---

[1] E. S. Smith et al., Nucl. Instrum. Meth. **A432**, 265 (1999).

[2] CLAS12 Technical Design Report v5.0, 2008.

[3] K. MacArthur, *CLAS Time of Flight System Forward Angle Scintillator Construction Manual*, University of New Hampshire, 1993.

[4] Caen, *Mod. V1290-VX1290 A/N, 32/16 Ch. Multihit TDC*, 2009.

[5] Caen, *Mod. V792/V792N 32/16 channel QDC*, 2009.

[6] V. Batourine et al., CLAS-NOTE-2004-016: Measurement of PMT Time Resolution at Kyungpook National University, 2004.

[7] S. Armstrong and E. Smith, CLAS-NOTE-91-018: Magnetic Shielding of Photomultiplier Tubes

in the CLAS TOF, 1991.